Cylindrical Polarimetric Phased Array Radar: Beamforming and Calibration for Weather Applications

Caleb Fulton, *Senior Member, IEEE*, Jorge L. Salazar, *Senior Member, IEEE*, Yan Zhang, *Senior Member, IEEE*, Guifu Zhang, *Senior Member, IEEE*, Redmond Kelly, John Meier, Matt McCord, Damon Schmidt, Andrew D. Byrd, *Student Member, IEEE*, Lal Mohan Bhowmik, *Student Member, IEEE*, Shaya Karimkashi, *Member, IEEE*, Dusan S. Zrnic, *Life Fellow, IEEE*, Richard J. Doviak, *Life Fellow, IEEE*, Allen Zahrai, Mark Yeary, *Fellow, IEEE*, and Robert D. Palmer, *Fellow, IEEE*

***Abstract*— Future weather radar systems will need to provide rapid updates within a flexible multifunctional overall radar network. This naturally leads to the use of electronically scanned phased array antennas. However, the traditional multifaced planar antenna approaches suffer from having radiation patterns that are variant in both beam shape and polarization as a function of electronic scan angle; even with practically challenging angle-dependent polarization correction, this places limitations on how accurately weather can be measured. A cylindrical array with commutated beams, on the other hand, can theoretically provide patterns that are invariant with respect to azimuth scanning with very pure polarizations. This paper summarizes recent measurements of the cylindrical polarimetric phased array radar demonstrator, a system designed to explore the benefits and limitations of a cylindrical array approach to these future weather radar applications.**

***Index Terms*— Calibration, conformal arrays, digital phased array radar (PAR), dual polarization, phased arrays.**

I. Introduction

WHILE radar polarimetry with accurate multiparameter measurements has become a matured technology in weather applications, there is a growing need for fast data updates for severe weather observations and quantification. Currently, it takes about 5 min for the WSR-88D to complete a volumetric scan. The 5-min data update time is too slow to reliably capture severe weather events such as tornadoes and downbursts, which sometimes last only a few minutes. It is desirable to have radar data with a higher temporal resolution ($\leq$1 min) so that detailed evolutions of severe storm phenomena can be revealed and tracked. There is also evidence that if quickly updated data are assimilated into numerical weather prediction models, then the forecasting accuracy improves significantly [1]. Rapid adaptive updates are difficult to achieve operationally with a mechanically scanning dish antenna radar, although a few research radars are capable of performing faster scans for short periods of time [2], [3]. The need for fast data updates points to using advanced radar technology such as the phased array radar (PAR), which has an agile beam that steers electronically and quickly [4]. The PAR is also needed for multimission capabilities, in which weather surveillance, air traffic control, and target detection and recognition are all performed within a single network, e.g., a multifunction PAR (MPAR) [5]. Since the national radar network of WSR-88Ds was upgraded by 2013 with dual-polarization capability, the leading candidate for future weather observation and/or air surveillance will be a polarimetric PAR (PPAR) [6]. The following section summarizes the antenna-related challenges and derived requirements for polarization and sidelobe performance for the MPAR application.

A. MPAR Antenna Challenges and Past Research Efforts

PPARs have been developed for NASA and military missions [7], but with limited scanning angles and aperture sizes due to technical challenges and high cost. For ground-based weather surveillance, however, it is difficult to use PPAR technology because of the requirement for highly accurate polarimetric radar measurements, given that there are limited resources for the development of this technology. The technical challenges include: 1) using a 2-D wide-angle scan (versus 1-D narrow angle scan in polarimetric NASA and military missions) and 2) achieving a high level of accuracy in polarimetric radar measurements. Specifically, in wide-angle scanning, the beam broadens considerably at large scan angles and cross-polarization isolation deteriorates appreciably [6]. This makes it difficult to achieve system-level goals, which include a differential reflectivity (Z_{DR}) error $\leq$0.2 dB (ideally 0.1 dB) and a correlation coefficient (ρ_{HV}) error $\leq$0.005. The specific differential phase K_{DP} should also be accompanied by less than a 3° std. dev. in the differential phase bias between H and V, ϕ_{DP}.[1] These are in addition to the requirements for target detection and low sidelobes [8]–[10]. Table I summarizes these requirements for any candidate MPAR-like system. It should be additionally noted that the "objective" two-way

Manuscript received June 29, 2016; revised December 4, 2016; accepted January 6, 2017. Date of publication February 13, 2017; date of current version March 17, 2017. This work was supported by the NOAA National Severe Storms Laboratory under Cooperative Agreement NA11OAR4320072.

The authors are with the University of Oklahoma's Advanced Radar Research Center, Norman, OK 73019 USA (e-mail: fulton@ou.edu).

Color versions of one or more of the figures in this paper are available online at http://ieeexplore.ieee.org.

Digital Object Identifier 10.1109/TGRS.2017.2655023

[1]This is at a spectrum width of 4 m/s, SNR > 20 dB, PRF = 321 Hz, and 16 samples

TABLE I

ROUGH MPAR REQUIREMENTS: STRAIGHTFORWARD (LIGHT GRAY), MANAGEABLE (MEDIUM GRAY), AND CHALLENGING (DARKER GRAY)

Antenna metric/property	Threshold	Objective (if better)
AZ and EL beamwidths, deg.	1.0	
AZ scan range, deg. (if 4 face planar)	-45 to 45	
EL scan range w/polarimetry, deg.	-1 to 20	-1 to 30
EL scan range, other functions, deg.	to 60	
Scan resolution, deg.	1.0	0.5
Close-in sidelobes (two-way), dB	<-34 (first 3)	< -54 (first)
Mid-range sidelobes (two-way), dB	< -52 dB	< -54@2° to < -68@10°
Far-out sidelobes (two-way), dB	< -52 dB	< -80 dB beyond 10°
Bias in Z_{DR} estimate, dB	< 0.1	
Bias in ρ_{HV} estimate	< 0.005	< 0.001
Error in ϕ_{DP} estimate, std. dev.	< 3°	
H and V matching @ beam peak, dB	< ~0.05	
H and V matching @ -20 dB, dB	< 1	< 0.5
Cross-polar isolation (ATSR), dB	< -22	< -25
Cross-polar isolation (STSR), dB	< -40	< -45

TABLE II

PLANAR VERSUS CYLINDRICAL TRADE SPACE OVERVIEW: GOOD (LIGHT GRAY), MANAGEABLE (MEDIUM GRAY), AND CHALLENGING (DARKER GRAY) CHARACTERISTICS

Property	Cylindrical array	Multi-face planar array
Scan variation in pattern	EL only	AZ and EL
Cross-polarization	good everywhere	worse in intercardinal planes
Scan-dependent cal.	simpler	more complicated
Sidelobe control	more difficult	simpler
Pattern matching	more complicated	simpler
Scan impedance	varies per column	varies with scan angle
Design heritage	weak	mature
Beamformer complexity	higher	standard
Number of elements	comparable	comparable
Sector/face independence and isolation	worse	good isolation; nominally independent

sidelobe levels [transmit (Tx) + receive (Rx) cascaded] as they appear in Table I are significantly less stringent than what is ideally desired for a weather radar, where close-in sidelobes must be better than −70 dB, lowering to −110 dB for larger angles [11]. In terms of polarization purity, the levels of accuracy in Table I require highly matched copolarized H- and V-polarized beam patterns (99%) and low cross-polarized levels (e.g., −25 dB for alternate transmission and −45 dB for simultaneous transmission) [12], [13] that have been achieved with dish antenna radar systems due to their low cross polarization and a null on the beam axis—PPAR technology cannot currently realize these levels of accuracy over the desired azimuth (AZ) and elevation (EL) ranges.

A planar PPAR (PPPAR) has inherent limitations in making accurate polarimetric measurements because of its changing beam characteristics with scan angle. For a PPPAR, four faces are normally used to cover the 360° in AZ. Because the antenna faces and their broadside directions are fixed, the beam and polarization characteristics change depending on the electronic beam direction with an angular coverage of [−45°, 45°]. This causes geometrically induced cross-polarization coupling [6], [14], as well changing beamwidth and mismatches in copolarized power and beam shapes, limiting the fidelity of scientific observations. As shown in [15, Fig. 5], the PPPAR has an elliptical copolarized pattern and has a coaxial cross-polarized peak that can be as high as 12.4 dB below the copolarized peak when scanning off broadside. This is due to the asymmetry caused by beam steering off the principal planes and is not acceptable for polarimetric measurements of weather, unless accurate calibration is done for every single beam direction. Correction of the cross-polarized bias in a PPPAR is feasible [6], [16], [17] and has been or is currently being demonstrated on several smaller systems [9], [18], [19]. However, practical calibration over a thousand different beam frequency combinations in either the near field or far field of larger systems is troublesome and has not yet been demonstrated; near-field approaches may be limited by probe correction accuracy and far-field approaches require excessively large distances to stay in the far field of apertures with larger diameters (on the order of $2D^2/\lambda$, a few kilometers). A way to naturally avoid the cross-polarized coupling in a PPPAR is to use a pair of ideal collinear magnetic and electric dipoles [14], [20], but there is still the issue of unmatched beam patterns that has not yet been addressed. In general, there is still work to be done on optimizing PPPAR performance from the element design standpoint, but it is unlikely that a "calibration-free" design will emerge from these efforts.

B. CPPAR Concept and Paper Overview

One of the most promising concepts for eliminating many of these PPPAR-related challenges is that of a cylindrical PPAR (CPPAR). For weather radar applications, CPPAR beams are scanned by commutating a roughly 90° active sector, with the radiated beam always staying broadside to the sector [21]. This not only simplifies the process of calibrating each beam to have matched copolarized patterns but also offers the potential for very low cross-polarization owing to natural pattern symmetry characteristics. In fact, a well-designed CPPAR can maintain a symmetric copolarized pattern as well as a null in its cross-polarized patterns, just like the polarimetrically accurate WSR-88D [17], [21].

Unfortunately, there are no existing large-scale CPPAR systems on which researchers could explore the practical benefits and challenges of a cylindrical approach to MPAR. There are not only questions about practically achievable polarization and beam shape accuracies but also CPPAR-specific system-level practical challenges. The emerging trade space is summarized in Table II. Cylindrical arrays suffer from the potential for strong surface and creeping wave effects, as well as the difficulty of achieving low sidelobes. Even from a pattern-only perspective that neglects the system-level implications of transceiver electronics, backend architecture, calibration, and operational constraints, there are very few available large-array (unit cell) and pattern synthesis techniques for complex antenna element geometries within a cylindrical array framework [20]. This makes it difficult to even *simulate* electromagnetically accurate cylindrical array patterns in an ideal system. This in turn has made it difficult for the MPAR community to

Fig. 1. OU/NSSL CPPAR demonstrator on turntable at far-field test site.

quantify the tradeoffs in Table II. Despite both architectures having a similar number of elements in total [21], important practical questions remain about a generic CPPAR's sector-to-sector isolation, mechanical/integration costs associated with nonplanar superstructures, and independence between sectors in terms of beam pointing direction.

To demonstrate the basic feasibility of CPPAR with a real system, the University of Oklahoma (OU) has teamed with the National Severe Storms Laboratory (NSSL) to develop a CPPAR demonstrator, as shown in Fig. 1 [22]. The 2-m-diameter, 2-m-tall cylinder features columns of patch antennas that are frequency scanned in EL, with each column being driven by a pair of digital transceivers [23]. All beams are scanned digitally in AZ on both Tx and Rx, using circuitry that is similar to [24]. This flexible and relatively low-cost approach to beamforming has allowed the OU/NSSL team to begin to separately explore electronic calibration and beamforming challenges, that is, determining and ensuring the proper amplitude and phase on each analog and digital electronics channel, in addition to answering questions surrounding the pattern-related effects described above. This paper summarizes the early results of the latter study, and demonstrates that a cylindrical approach to MPAR can mitigate several pattern-related risks. In particular, copolarized beam pattern matching, cross polarization, sector-to-sector isolation, and sidelobe levels are detailed.

Section II provides a high-level overview of the CPPAR demonstrator, highlighting its features and limitations as well as its far-field testbed and overall calibration approach (updating the earlier plans in [22]). Section III then details the relevant aspects of the antennas on the CPPAR demonstrator, motivating and then discussing the current approaches to pattern synthesis as well as the need for precise knowledge of embedded element patterns. This is motivated by the simulation-based study in [25]. Section IV shows the resulting radiation patterns obtained through initial measurements and discusses what they do and do not confirm about the trade space in Table II. In general, while much of this paper will help the overall MPAR community better understand the broader antenna challenges of Table I and will directly inform the general trade space in Table II, some of the challenges and solutions detailed herein are specific to design choices made for the CPPAR demonstrator; these are identified clearly throughout the paper. Finally, Section V summarizes this paper as well as future research opportunities.

II. CPPAR Demonstrator

The CPPAR demonstrator's antenna array consists of 96 columns of 19 dual-polarized, frequency-scanned, aperture-coupled, and stacked patch antennas that are designed to operate from approximately 2.7 to 3.0 GHz [23]. Currently, 48 of the columns are populated on the system. A stripline feed structure for each polarization excites the patches from coaxial cable ports on the bottom of each column, with the resulting beam scanning from approximately 0° EL at 2.74 GHz to 13° EL at 2.95 GHz. Higher angles are possible, but far-field testing has been limited to lower EL angles. The 3-dB beamwidth in EL is approximately 6° and the 3 dB AZ beamwidth ranges from approximately 5.2° to 6°, depending on the choice of amplitude tapering during digital beamforming. The spacing in AZ between columns is 3.75° or 65 mm at the array face, with a spacing between elements on the column of 70 mm. As explained further in Section III, these relatively large element spacings lead to large mismatches between embedded horizontal (H) and vertical (V) copolarized patterns that must be taken into account.

The decision to use frequency steering for EL scanning was simply to save cost by eliminating the need to place active Tx/Rx (T/R) modules on each element in the array; it is not a viable approach for MPAR. However, the focus of the CPPAR demonstrator's pattern studies are on the AZ dimension, where unlike the EL dimension there are much more significant differences between a CPPAR and a PPPAR. In fact, the engineering trade spaces for EL scanning on a PPPAR and a CPPAR are nearly identical when it comes to polarization and sidelobes, especially over the narrow weather radar EL range of 0–20°; the only notable difference is the inability to have a CPPAR tilted back to achieve better EL coverage.

To enable flexible AZ beamforming, each polarization of each of the 32 active columns is independently driven by its own digital transceiver, as shown in Fig. 2(b) and detailed in [22]; system-level radar performance estimates are also detailed therein. The number of active columns is scalable to the full 96 columns, but the current 32 columns are sufficient to explore pattern-related effects in the full system. For both the demonstrator and any viable CPPAR for MPAR applications, digital beamforming of the columns (if not additionally among subarrays or even elements on each column) is a practical requirement to avoid the need for exception-

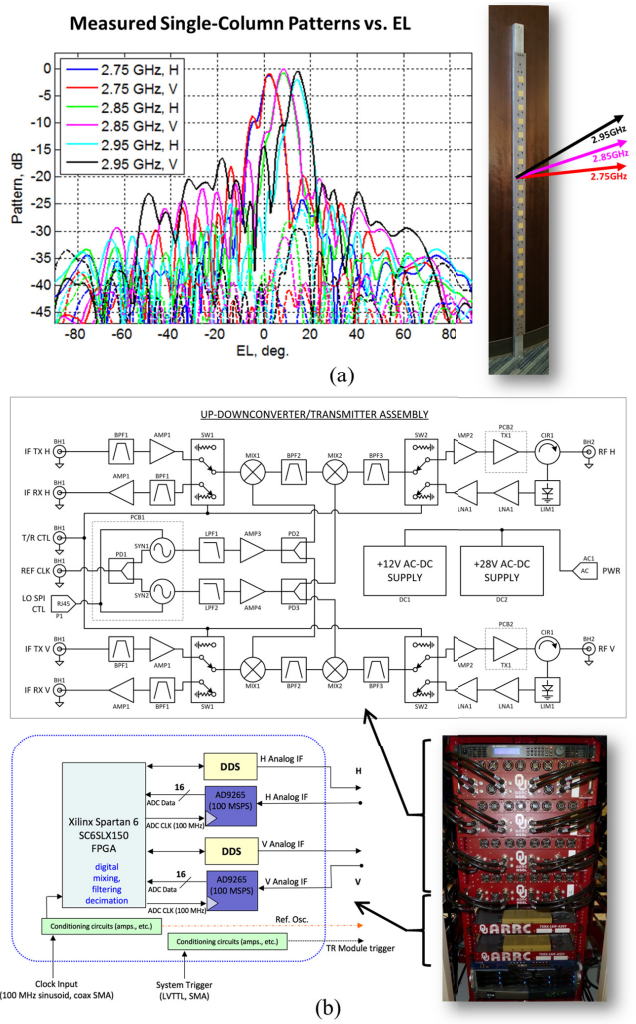

Fig. 2. Important CPPAR demonstrator Subsystems. (a) Antenna from [23] with measured EL patterns and (b) RF and digital transceiver channel block diagram from [26].

ally complex analog/RF switch and beamforming networks. Each digital transceiver consists of a pair of RF frontends, up/downconverters (UDCs), and digital IF transceivers, the block diagrams of which are also shown in Fig. 2(b). Within the IF transceivers, direct digital synthesizers (DDSs) are utilized to generate digital waveforms for the radar. DDSs allow for smooth communication between array nodes and efficient beamsteering in this application, so long as a synchronization technique ensures the operation of an accurate master clock.

For the CPPAR demonstrator, two AD9954 DDS subsystems and one field-programmable gate array (FPGA) controller make up each column's DDS, as detailed in [26]. This particular DDS is a 14-b device that supports 400 MSPS and a tuning granularity of 0.093 Hz to create phase-coded waveforms; currently, linearly frequency modulated or continuous wave (CW) pulsed waveforms are used. A host computer provides a master clock to all nodes and each node serially interfaces with the host. Additionally, the host can communicate with each node over an Ethernet connection using a trivial file transfer protocol. The FPGA is configured with a Microblaze subsystem that interfaces it with the host, DDSs, and the transceiver as analog-to-digital converters (as discussed in the next paragraph). Two channels of the transmitted waveform are delivered to UDCs, centered at an IF of 70 MHz.

Each UDC consists of the necessary filters, amplifiers, local oscillators (LOs), and mixers to convert between this 70-MHz IF and the operating band. The LOs are each independent but are synchronized to each other in that they share the same 10-MHz system reference for their integer-N phase-locked loops. In the Tx frontend, each polarization on each column is driven by an 80-W class C GaN amplifier, connected to the antenna through high-power T/R switches and low-loss RF coaxial cables. For reception of the received echoes, each Rx frontend includes a limiter and a low-noise amplifier (LNA), with an optional "low gain" LNA bypass mode to support the advanced calibration routines highlighted in Section II-A.

Each UDC then converts the Rx signals into 70-MHz IF signals of the H and V channels for each antenna. Likewise, two analog-to-digital converters digitize the incoming the IF signals within the digital IF transceivers. Each is rated at 16 b and is clocked at 100 MHz to achieve bandpass sampling, rather than subsampling as in [27]. To achieve low-cost lightweight digital receiver modules for weather radar applications, this undersampling strategy has been proved effective [28], [29]. Following the sampler, two digital mixers and a pair of cascaded integrator-comb filters, a pair of compensation finite impulse response (CFIR) filters, and a pair of pulse-shaping finite impulse response (PFIR) filters produce the in-phase (I) and quadrature (Q) components of the baseband signal, respectively. Hence, the FPGA in the digital transceiver ingests each bit stream and demodulates each to provide the I and Q samples for the H and V channels. Each received pulse is streamed through USB 3.0 connections to hard drives for postprocessing. The physical design of system is carefully organized such that the clocks entering all FPGAs are in phase with each other. Similarly, reference clocks from the FPGA to each DDS are devised to be in phase with each other. Careful planning matches the clocks entering and leaving the DDSs, but Tx triggers for each DDS throughout the array need to be generated synchronously as well. Again, the UDCs are also synchronized based on the same 10-MHz system reference used to drive the digital side of the system.

A. CPPAR Testbed and Calibration

As with any active phased array, the successful testing and eventual operation of the CPPAR demonstrator relies on calibration techniques to measure and remove errors in its electronic channels, in addition to corrections that must be made for mutual coupling (MC) and other electromagnetic effects associated with its specific antenna design. The primary sources of electronics errors are small static mismatches in channel gains and phases as well as temperature-dependent amplitude and phase drifts. The phase drifts are primarily attributable to the LOs within the UDCs being independent (but still frequency locked) and the amplitude drifts are mostly caused by power amplifier heating and cooling. The antenna-specific and static electronic error corrections—collectively denoted here as *initial calibration* steps—have been the focus

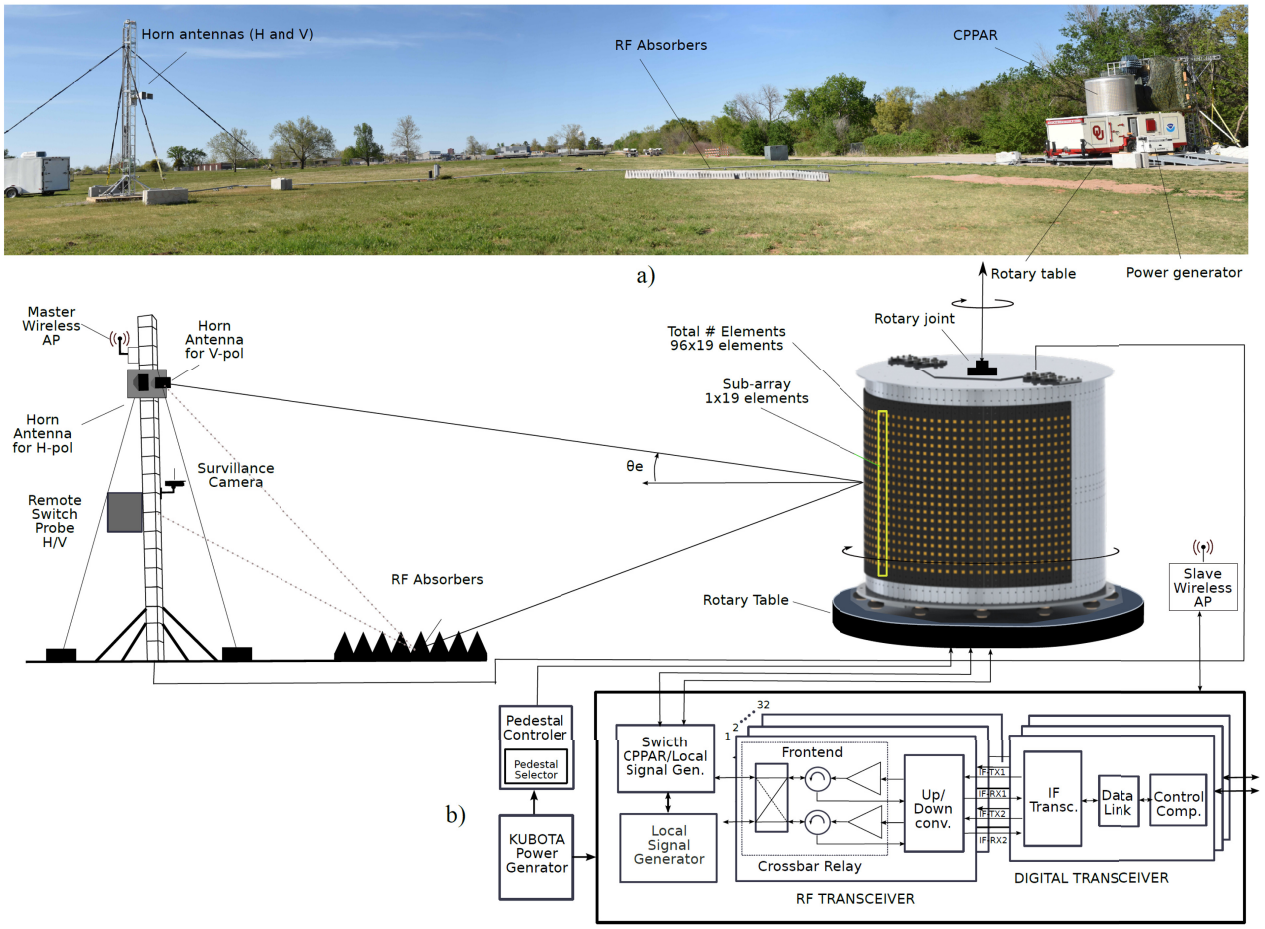

Fig. 3. CPPAR test setup for far-field antenna measurements. (a) Picture of the CPPAR in the ARRC far-field range facility. (b) Block diagram representation of the CPPAR test setup showing all measurement components.

of the study thus far and are thus detailed here; further research is underway to address slow time and temperature dependencies using *in situ* calibration techniques derived from the processes described below.

The CPPAR demonstrator's initial calibration and pattern measurements are facilitated by the far-field testbed shown in Fig. 3, where the CPPAR sits on top of a rotating platform with open-loop position control. The early plans outlined in [22] are revisited here in the context of this more sophisticated testbed. The demonstrator operates as a pulsed coherent radar system and the most accurate way to extract the amplitude and phase information of each column is to sample the far field of each pulse directly. This is accomplished with the far-field tower shown in Fig. 3, which is placed 45.7 m from the center of the CPPAR. The tower has two linearly polarized horn antennas connected through cables to a switch box on the tower that connects through a long low-loss RF cable back to the CPPAR installation. The horn antennas have a cross-polarized isolation measured to be better than -40 dB, with matching of the copolarized beams ensured through mechanical alignment. The horns can be manually raised and lowered by a crank to measure an EL angle between 0° and approximately 6.0°. The long RF cable connects through a rotary joint off of a tower backing the CPPAR to another switch box that connects to a phase-locked reference source for Rx measurements, where signals received on each of the columns are digitally stored for offline processing (e.g., calculation of patterns). For Tx measurements, one polarization of one of the demonstrator's active transceiver channels is used to store the signals received from the far-field horn when the active sectors are all transmitting simultaneously. Four such channels (corresponding to the two outer columns) have been dedicated to current and future calibration purposes, and therefore, $N_A = 30$ of the 32 active columns are used in the pattern measurements herein. Finally, a structure that is coated with absorbing foam backs the CPPAR itself to minimize reflections of the tower that would not exist in an operational system, and absorbers are additionally placed along the specular patch region on the ground between the CPPAR and the far-field tower.

The overall initial calibration (alignment and pattern measurement) process is summarized in Fig. 4. It is further explained below after a discussion on the physical measurement processes. As the CPPAR rotates on its turntable, an absolute positioner records the current AZ angle, while the CPPAR samples the complex pattern values. During Tx measurements of the column patterns, at each new AZ position, the demonstrator fires 10-μ_s unmodulated pulses at zero phase and full power on each column sequentially. The signals received by one of the far-field horns (one per polarization)

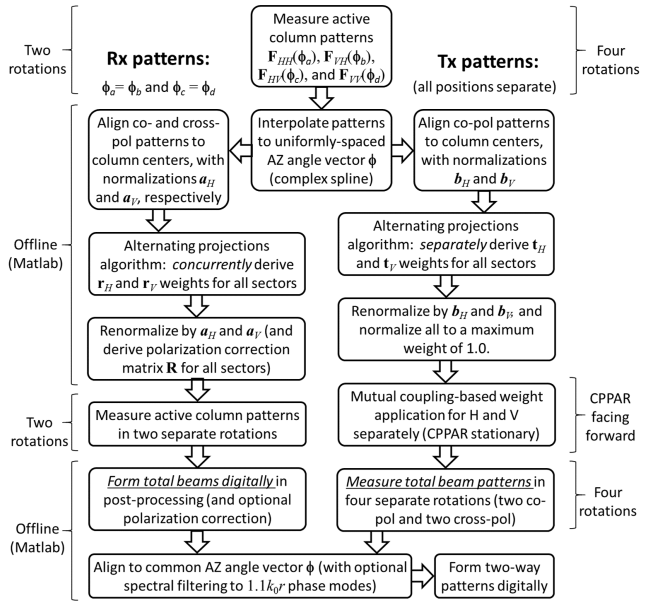

Fig. 4. CPPAR calibration and pattern measurement process overview.

are recorded by a spare transceiver in a pulse-synchronous manner. During Rx measurements, the phase-locked reference provides a CW reference plane wave at the face of the CPPAR of either H or V polarization from the far-field horns and the digital receivers record raw I/Q samples for each position-tagged pulse on each polarization and each column. For each pulse/position on either Tx or Rx, the I/Q data are averaged within the pulse to achieve an estimate of the pattern for each column.

For Rx patterns, the initial calibration process begins with two CPPAR rotations with the H and V horn selected, respectively. This allows for the measurement of the active column patterns $\mathbf{F}^R_{\mathrm{HH}}(\phi_a)$ and $\mathbf{F}^R_{\mathrm{VH}}(\phi_a)$ during the first rotation and $\mathbf{F}^R_{\mathrm{HV}}(\phi_b)$ and $\mathbf{F}^R_{\mathrm{VV}}(\phi_b)$ during the second. Here, ϕ_a is a vector of positions for the first rotation and ϕ_b holds the positions for the second. The active column patterns are functions of these positions and are also depicted (and stored) as vectors that are indexed by the active channel. Their first subscript denotes the CPPAR polarization port and the second subscript indicates the far-field horn polarization. These active column patterns capture all MC effects, automatically include the relative gain and phase of the active electronics in each channel, and for the demonstrator also reflect the fact that each column is frequency-scanned in EL according to the current radar center frequency. For Tx pattern measurements, which are performed separately, four rotations are required to capture $\mathbf{F}^T_{\mathrm{HH}}(\phi_a)$, $\mathbf{F}^T_{\mathrm{VH}}(\phi_b)$, $\mathbf{F}^T_{\mathrm{VH}}(\phi_c)$, and $\mathbf{F}^T_{\mathrm{VH}}(\phi_d)$, because only one far-field channel is available at a given time; this leads to four different position vectors (ϕ_a, ϕ_b, ϕ_c, and ϕ_d). In general, because the electronics and positions are different on Tx and Rx, no assumptions are made about reciprocity and Tx and Rx patterns are treated separately. In a larger fully active CPPAR, these active embedded element patterns could be measured using traditional cylindrical near-field scanning techniques [30].

Once the active column patterns are captured during the initial rotations for offline processing, the patterns are all complex spline interpolated to a uniformly spaced vector of points ϕ so that they can be commonly indexed on a grid that includes column center locations (every 3.75°). The resolution of the original patterns is typically a few tenths of a degree, more than sufficient for the phase mode bandwidth of the patterns (see also Section IV), and the resolution of ϕ is chosen similarly. In what follows, the $\mathbf{F}_{XY}$ ($X,Y = H$ or V) patterns are sampled on these uniform AZ values, of which there are N_{AZ}.

The channel alignment process consists of digital normalization of the measured patterns. This is currently implemented mathematically by first sampling the complex copolarized patterns at their column centers and storing their inverses in vector form as *alignment weights* $\mathbf{a}_H$ and $\mathbf{a}_V$ for Rx patterns and $\mathbf{b}_H$ and $\mathbf{b}_V$ for Tx patterns. These weights represent complex normalization factors that make it so that each column's complex pattern, evaluated at the center of each column's pointing angle, is identical. For example, the value of the nth entry in $\mathbf{a}_H$ would be $a_{H,n} = 1/F^R_{\mathrm{HH},n}(\phi_n)$, where $F^R_{\mathrm{HH},n}$ is the nth entry of $\mathbf{F}^R_{\mathrm{HH}}$ and ϕ_n is the AZ angle where the nth column is facing the far-field tower. The *aligned patterns* are then given by

$$\mathbf{F}^{R_A}_{\mathrm{HH}} = \mathbf{F}^R_{\mathrm{HH}} \odot \mathbf{a}_H \quad \mathbf{F}^{R_A}_{\mathrm{HV}} = \mathbf{F}^R_{\mathrm{HV}} \odot \mathbf{a}_H \tag{1a}$$

$$\mathbf{F}^{R_A}_{\mathrm{VV}} = \mathbf{F}^R_{\mathrm{VV}} \odot \mathbf{a}_V \quad \mathbf{F}^{R_A}_{\mathrm{VH}} = \mathbf{F}^R_{\mathrm{VH}} \odot \mathbf{a}_V \tag{1b}$$

for Rx operation and

$$\mathbf{F}^{T_A}_{\mathrm{HH}} = \mathbf{F}^T_{\mathrm{HH}} \odot \mathbf{b}_H \quad \mathbf{F}^{T_A}_{\mathrm{VH}} = \mathbf{F}^T_{\mathrm{VH}} \odot \mathbf{b}_H \tag{2a}$$

$$\mathbf{F}^{T_A}_{\mathrm{VV}} = \mathbf{F}^T_{\mathrm{VV}} \odot \mathbf{b}_V \quad \mathbf{F}^{T_A}_{\mathrm{HV}} = \mathbf{F}^T_{\mathrm{HV}} \odot \mathbf{b}_V \tag{2b}$$

for Tx operation. Here, the $\odot$ symbol indicates a simple Hadamard (element-wise) product. These patterns are then sent to the alternating projections (AP) algorithm described in Section III-B and indicated in Fig. 4, which produces *weight matrices* $\mathbf{W}^R_H$ and $\mathbf{W}^R_V$ for H and V Rx patterns and $\mathbf{W}^T_H$ and $\mathbf{W}^T_V$ Tx patterns. These matrices are each $N^R_S \times N_A$ (or $N^T_S \times N_S$) in size, where $N_A = 30$ is the number of antenna columns and N^R_S (N^T_S) is the number of possible active sectors within the populated demonstrator face for a fixed number of Rx columns (N_R) or Tx columns (N_T) for forming each possible beam. Currently, $N_R = 22$ for lower sidelobes and $N_T = 24$ for maximum Tx power. The rows of the weight matrices contain weights to be mathematically applied to the aligned patterns to produce the sector beams.[2] For example, the first row of the Rx weight matrix $\mathbf{W}^R_H$ consists of the weights to be applied to the first sector or the first N_R elements, followed by $N_A - N_R$ zeros. These weights must be applied *in addition* to the aforementioned alignment weights in order to ensure that the proper amplitude and phase are enforced in the presence of transceiver errors, since the weights themselves are derived using aligned patterns from 2. Mathematically, then, the final *calibration weights* are thus given by

$$\mathbf{A}_H = \mathbf{W}^R_H \mathrm{diag}(\mathbf{a}_H) \quad \mathbf{A}_V = \mathbf{W}^R_V \mathrm{diag}(\mathbf{a}_V) \tag{3a}$$

$$\mathbf{B}_H = \mathbf{W}^T_H \mathrm{diag}(\mathbf{b}_H) \quad \mathbf{B}_V = \mathbf{W}^T_V \mathrm{diag}(\mathbf{b}_V) \tag{3b}$$

[2]These weights are currently sector dependent, owing to the need to minimize the impact of mechanical variations in the first batch of antennas; further research with a new batch of antennas will test the practical limitations to the pure commutation of weights.

where diag(**x**) is a diagonal matrix with the entries of **x** along its diagonals. For Rx patterns, these are the final complex weights that are digitally applied to all subsequent active column signals during offline processing, forming the overall sector beams upon summation (see Section III-B for further discussion on sector beam processing).

For Tx patterns, these complex calibration weights must be applied digitally through the DDS channels, using the final calibration weights for a given sector, as the amplitudes and phases of the baseband waveforms on each column. However, because the power amplifiers are highly nonlinear, this process must be performed iteratively based on feedback to ensure that the amplifiers are operating at the desired amplitude and phase relative to the values they had during the measurement of $\mathbf{F}_{\mathrm{VV}}^{T}$ and $\mathbf{F}_{\mathrm{HH}}^{T}$. In the current testing, this is accomplished through an MC algorithm that was first developed and demonstrated in [31], was combined with a related approach for large planar arrays (from [32]) in [33], and has been modified for use on the CPPAR demonstrator. First, all Rx frontends have the LNAs bypassed so that the receivers will not saturate from nearby transmitting columns. An initial coupling matrix **C** from each Tx column (matrix column index) to each receiver (matrix row index) is made, immediately following the initial active column pattern measurements and using the exact same sequential firing of each transmitter. For each polarization separately, a sector weight vector **c** is selected from among the columns of $\mathbf{B}_{H(V)}$ and applied directly to the DDS values' amplitudes and phases. The residual errors resulting from the nonlinear amplifier behavior are estimated by measuring a subsequent coupling matrix $\mathbf{C}'$ with the new DDS values and making an entry-by-entry comparison of [**C**diag(**c**)] and $\mathbf{C}'$ to determine what additional changes to Tx DDS values must be made for subsequent $\mathbf{C}'$ measurements to most closely match their mathematical ideal. After a few iterations (five here), the DDS values converge, with the transmitters then accurately reflecting the weights **C**. Further refinements and efficacy evaluations of this algorithm are underway, as are extensions to it that will allow it to be used for *in situ* calibration to track and digitally remove the aforementioned amplitude and phase variations over time and temperature (as was done in [31]).

Finally, for either Tx or Rx, subsequent CPPAR rotations allow for the measurement of full patterns. For Rx patterns, this is done through digital beamforming by applying the final calibration weights for each sector in parallel to the stored raw received signals at each rotation sample through offline processing; thus, all sectors are measured at once. For Tx patterns, sector patterns must be measured sequentially—the N_T columns of a given sector are activated, with the complex weights from the corresponding row $\mathbf{W}_H^T$ or $\mathbf{W}_V^T$ being applied to the DDSs for each of these columns. These pulsed signals are repeated continuously as the entire radar rotates, with the resulting signal from the far-field horn being stored using a dedicated channel's receiver. Again, four rotations are required for full Tx sector pattern measurements. The optional processes of polarimetric correction (PC) and phase mode filtering are discussed in Sections III and IV, respectively.

The above initial calibration process is generalizable to any digital phased array, either in near field or far field, and with the AP algorithm is particularly suitable for CPPAR applications. On the CPPAR demonstrator, like most active arrays, the resulting pattern accuracy is limited by the measurement setup as well as the electronic stability of the channels. With both the demonstrator and other future digital arrays, *in situ* calibration like the MC algorithm under development will be important in addressing stability concerns over time and temperature [34]. The CPPAR demonstrator Tx patterns are currently limited in accuracy by the need for multiple rotations to measure different polarizations, the accuracy of the developing MC algorithm, and leakage within the trailer from each transmitter to the dedicated Rx channel. These are discussed further in the context of the measurements themselves in Section IV.

III. Pattern Analysis and Synthesis

While the mechanics of channel alignment and stabilization may be similar between a future CPPAR and a PPPAR, a fundamental difference between them is the actual calculation of the weights for a given physical array configuration. Furthermore, there are distinguishing characteristics of the demonstrator that are potentially different than a future CPPAR owing to the particular element design choices made. In a large PPPAR, most of the sidelobe, polarization, and element design choices are driven by the fact that radiation patterns can be factored roughly into an element factor and an array factor ($EF \times AF$), where alignment accuracy dominates sidelobe performance, and angle-dependent polarization correction trades element design difficulty/realizability against practical measurement difficulties [18]. This is because relatively straightforward Fourier transform-like relationships dictate beam shape considerations and the current sheet behavior dictates polarization [35].

In a CPPAR, while cross-polarized patterns are more trivial to optimize for weather radar (where sectors are commuted, not electronically scanned), one must contend with the complications that arise from having the aforementioned factorization be replaced by a linear combination of commuted embedded element (column) patterns. When these patterns are complicated and/or difficult to predict, the processes of ensuring low sidelobes with matched copolarized beam shapes becomes much less trivial. Thus, there are two issues of importance in a CPPAR: 1) accurate prediction of embedded element or column patterns and 2) optimization of polarimetric pattern performance based on knowledge of these embedded patterns. These were explored in detail in [25] and separately in [36] from purely simulation perspectives, and the results and techniques used in [25] as applied to the present CPPAR demonstrator's measurements are summarized in the rest of this section.

A. Active Element (Column) Patterns and Simulations

The accurate simulation of the embedded column pattern (or element pattern, in general) on a CPPAR must take into account all MC, surface/creeping wave, and feedpoint impedance effects. To demonstrate low sidelobes (<-40 dB) and explore the limitations to front-to-back isolation, any approximations must be made very carefully.

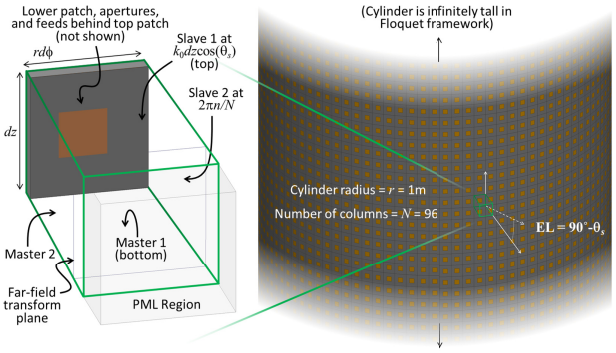

Fig. 5. CPPAR demonstrator unit cell analysis setup, showing the linked (master/slave) boundary conditions, perfectly matched layer, and overall geometry for the nth of N cylindrical phase sequence excitations.

While for any PAR it would be ideal to simulate the entire array in a robust electromagnetic framework, it is almost always computationally infeasible to do so when the array is sufficiently large or the element design is nontrivial. For the CPPAR Demonstrator, such "finite array" simulations have so far been limited to just seven columns [23], [36]. For a large PPPAR, it is possible to use infinite array simulations to approximate the large-array behavior through well-known unit cell approaches that make use of Floquet's Theorem to reduce the problem size to that of a single element for each scan angle [18].

Until recently, similar unit cell approaches for CPPARs were limited to simplified radiating elements on specific dielectric structures [20]. As first used in [25], detailed in [37], and summarized in Fig. 5, the present CPPAR demonstrator study has led to the development of a finite element method technique that makes use of a unit cell structure to accurately capture the radiated fields. The array is approximated as being infinitely tall (as in the PPPAR case) to capture MC effects versus EL scan angle, but the framework allows for the extraction of the raw embedded column pattern in AZ for each of these scan angles. The boundary conditions indicated in Fig. 5 allow for expedient simulation of the bracketed terms in the following equation for the electric field radiated by a column in a CPPAR:

$$\mathbf{E}(\theta_s,\phi)=\frac{1}{N}\sum_{k=0}^{N-1}\left[\sum_{n=0}^{N-1}\mathbf{E}(\theta_s,\phi-\frac{2\pi}{N}n)e^{j\frac{2\pi}{N}nk}\right]. \quad (4)$$

Here, $N = 96$ is the total number of columns (and thus the number of parallel simulations to run) and the identity itself comes as a result of basic Fourier series properties of the inherently periodic radiation in AZ. In fact, each of the bracketed terms can be used to calculate these Fourier series coefficients or *phase modes* [20]. The ϕ component of the field can be expressed using the phase mode coefficients a_m as

$$\mathbf{E}(\theta_s,\phi)\cdot\hat{\mathbf{n}}=\sum_{m=-\infty}^{\infty}a_m e^{jm\phi}. \quad (5)$$

The study in [25] simulated the CPPAR demonstrator's antenna within this framework, as shown in Fig. 6, in comparison with the simulation for a fixed EL angle. Clearly, there are both measured and simulated ripples on the H copolarized patterns near broadside to the column that do not appear

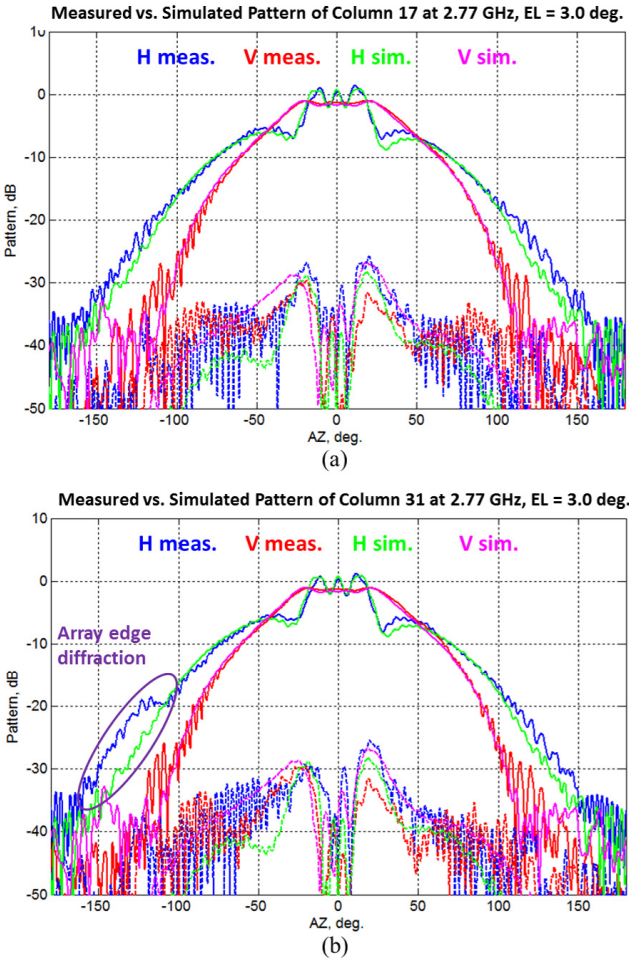

Fig. 6. Column pattern measurement versus simulation (a) near array center and (b) near array edge, where array edge diffraction effects are apparent but small.

in the V pattern. Analysis of the phase mode coefficients for H versus V revealed that there are certain modes of the H polarization that do not radiate and that this is caused by a surface wave on the grounded dielectric slab that leads to "phase mode blindness" in the CPPAR, as opposed to "scan angle blindness" that can often appear in PPPAR equivalents [38]. In other words, whereas traditional planar arrays with thick dielectric substrates and wide element spacing can suffer from the inability to radiate at certain angles from the array normal ("blindness"), cylindrical array structures with wide element spacing may exhibit the inability to radiate specific Fourier series components (phase modes) of the total azimuthally periodic radiation pattern from the cylindrical structure; this leads to ripples in the overall embedded pattern of each of the CPPAR columns. These ripples in turn complicate the pattern synthesis process by making it difficult to use proscribed excitations, necessitating the process in the following section. Importantly, the present results indicate that despite the CPPAR demonstrator being a finite cylinder (48 columns instead of 96), the unit cell simulations and the results in [25] have been largely validated; the only major discrepancies within and on the edge of the field of view are an small ripple in the patterns beyond $\pm 90°$ and a slight perturbation to the patterns of columns near the edge due

to edge diffraction. Further studies are being conducted to identify the sources of these small discrepancies between these patterns in anticipation of further measurements with a fully populated CPPAR, where backradiation can be truly verified.

B. Pattern Synthesis

Following the initial array alignment in (1) and (2), the most critical process for achieving low sidelobe levels and matched main beams for H- and V-polarized patterns is that of pattern synthesis, the determination of the optimal weight matrices in (3) and in Fig. 4. As discussed above, a simple "array factor"-based approach is insufficient for achieving low sidelobes with precise beam matching on a CPPAR with strong pattern variations within its main beam. As an example, the application of a 40-dB Taylor distribution using the simulated patterns of Fig. 6 to map to the phase and amplitude distribution on the demonstrator cylinder leads to close-in H copolarized sidelobes that are only −20 dB that improve to −40 dB near ±90° AZ, only to go back up to −32 dB at further out angles [25]. At the same time, the H copolarized main beam was so broadened by the pattern variations that the V patterns had to be manually weighted with 60-dB Taylor to lead to matched H and V copolarized beam shapes. The extent to which pattern variations in a general CPPAR lead to similar limitations is not clear, but an analysis of the previous results for other element types show similarity to those of the demonstrator's antennas [20]. Thus, in general, it was clear that application of *optimized* excitation coefficients to the antenna columns was needed, based on an evolutionary optimization algorithm of some sort (see [36]). In general, these algorithms work by optimizing pattern performance by iteratively adjusting the column (element) weights based on an algorithm that randomly (genetically) or deterministically refines the column weights based on guidance given by the pattern performance in the previous instance(s).

1) Overview and Goals: The current approach to these iterative/evolutionary optimizations on the CPPAR demonstrator is to use the AP technique [39], [40], as was done in [25] with the simulated patterns and as detailed herein for these measurements. The inputs to the algorithm are $\mathbf{F}_{\mathrm{HH}}^{R_A}$ and $\mathbf{F}_{\mathrm{VV}}^{R_A}$ from (1) for Rx and $\mathbf{F}_{\mathrm{HH}}^{T_A}$ and $\mathbf{F}_{\mathrm{VV}}^{T_A}$ from (2) for Tx. As highlighted in Section II-A, the goal is to generate the columns of the weight matrices $\mathbf{W}_H^R$ and $\mathbf{W}_V^R$ Rx and $\mathbf{W}_H^T$ and $\mathbf{W}_V^T$ for Tx to be used in (3), with the columns corresponding to different active sectors. The overall procedure is nearly identical between Tx and Rx, with the slight differences indicated in the following.

2) Assignment of Initial Weights: For a given sector's weights (the nth row of one of the $\mathbf{W}$s), denote the weight vectors for the mth iteration by $\mathbf{w}^m$, a row vector. The initial weight vector, critical to the success of the AP algorithm [39], is chosen for the first ($m = 1$) iteration according to a desired aperture illumination, where the kth weight of the active sector of $\mathbf{w}^1$ is given by

$$w_k^1 = W_k \cos\left(\left[k - \frac{N-1}{2}\right] d\phi\right)^E e^{-jk_0 \mathbf{r}_{k,n}\cdot\mathbf{u}_n}. \quad (6)$$

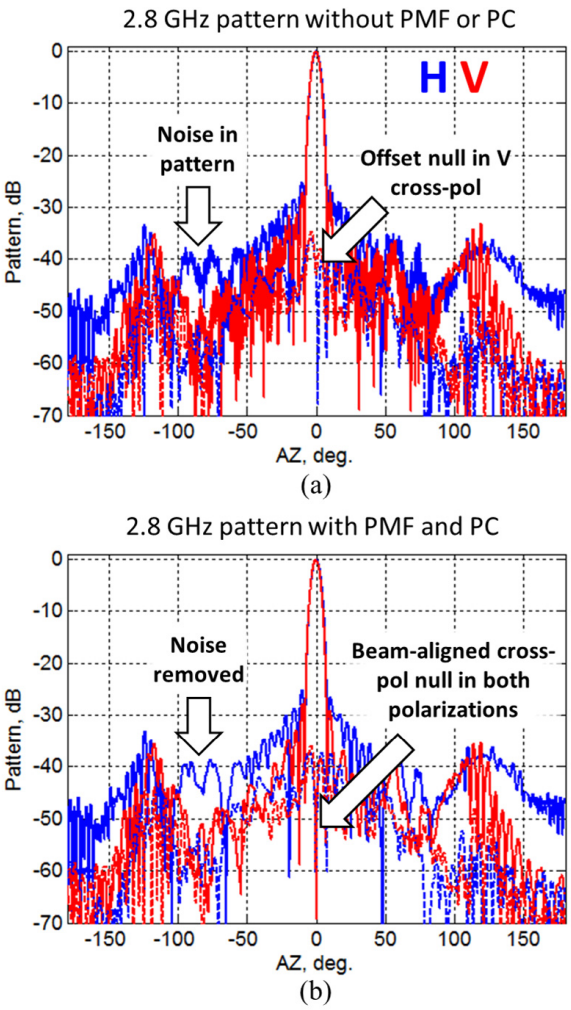

Fig. 7. Example of phase mode filtering and polarimetric correction (PC) on a 2.8-GHz Rx pattern (a) with and (b) without correction.

Here, N is the number of columns in the active sector, $d\phi$ is the angular column spacing, $\mathbf{r}_{k,n}$ is the phase center (vector) of the kth column in the nth active sector, and $\mathbf{u}_n$ is the unit vector pointing in the direction of the center of the nth active sector. The W_k are chosen according to a Taylor distribution whose nominal sidelobe level is different for H and V polarizations, and E is chosen to map the element density of the cylindrical aperture to that of a planar aperture. Its nominal geometrical value is $E = 1$, but for this paper, it is chosen as 1.5 to further taper the aperture in the presence of creeping/surface waves for both Tx and Rx patterns.

3) Iteration (Pattern Calculation and Mask-Based Modifications): At each iteration m, each copolarized pattern is calculated separately and digitally as $F^m(\phi) = \mathbf{w}^m\mathbf{F}(\phi)$, where $\mathbf{F}(\phi)$ is one of the aligned copolarized pattern vectors from (1) or (2) associated with the vector $\mathbf{w}^m$ in question, separately for the H and V polarizations. The AP algorithm then works by modifying these resulting patterns according to a masking function $M(\phi)$ that dictates the maximum allowable sidelobe level versus angle. Mathematically, the

new "desired" copolarized patterns are calculated as

$$F^m_{d(X)}(\phi) = \begin{cases} F^m_{XX}(\phi) & \text{if} |F^m_{XX}(\phi)| < M(\phi) \\ \dfrac{F^m_{XX}(\phi)}{|F^m_{XX}(\phi)|} M(\phi) & \text{if } |F^m_{XX}(\phi)| \geq M(\phi) \end{cases} \quad (7)$$

where X is either H or V. The mask M is defined in a piecewise linear fashion in the logarithmic (dB) domain and is tailored to fit a specific beam shape and sidelobe profile, centered at the active sector's center, which is based on the ultimate goals in Table I and is identical for H and V; this is further discussed in the context of the individual results in Section IV and detailed in [25] for the simulated embedded column patterns therein. The above operation ensures that the sidelobes are kept below the mask M at each iteration, while carefully preserving a desired beamwidth on the main beam. For Rx patterns only, the desired copolarized patterns are additionally modified so that the desired V copolarized patterns are identical to the H copolarized pattern within the main beam region indicated by ψ for the nth sector. In other words, the ideal V copolarized pattern is modified to be

$$F^m_{d(V)}(\phi) = \begin{cases} F^m_{d(H)}(\phi) & \text{if } \phi \in \psi \\ F^m_{d(V)}(\phi) & \text{else.} \end{cases} \quad (8)$$

4) Iteration (Mapping Back to Realizable Patterns): These "ideal" modified patterns F_d are then projected back to physically realizable patterns, or linear combinations of the entries in the aligned patterns of (1) or (2), through a weighted least squares process. For polarization X, the resulting weights for the next iteration are given by

$$\mathbf{w}^{m+1} = (\mathbf{F}^{\mathrm{T}}_e \mathbf{W} \mathbf{F}_e)^{-1} \mathbf{F}^{\mathrm{T}}_e \mathbf{W} \mathbf{F}^m_{d(X)} \quad (9)$$

where $\mathbf{F}^m_{d(X)}$ is a column vector holding the sampled desired pattern of the mth iteration for polarization X with N_{AZ} entries, $\mathbf{F}_e$ is a $N_{AZ} \times N_R$ or $N_{AZ} \times N_T$ matrix for Tx and Rx, respectively, holding the sampled aligned patterns from (1) or (2) for the current (nth) sector, and $\mathbf{W}$ is a $N_{AZ} \times N_{AZ}$ diagonal matrix specifying the relative importance of the mask fitting at each angle, indexed by the diagonal entries. Different weights result for Tx and Rx, for each polarization and for each sector.[3] The entries of $\mathbf{W}$ are currently given by samples of $[M(\phi)]^\alpha$ for a fixed α at each of the AZ samples along ϕ, with $\alpha = -0.6$. Higher values of α emphasize matching within the main beam and lower values emphasize satisfaction of sidelobe constraints.

5) Final Weights and DBF: For both Tx and Rx, the above algorithm is iterated back and forth (between ideal pattern and realizable excitations) a number of times (currently 16 times), resulting in patterns that approximate the mask as best as is practically realizable. If the final Rx weight vectors for the X polarization are stacked sector by sector (by n) as $\mathbf{W}^R_X$, then the final sector beams that are calculated digitally in the postprocessor are given by the AZ samples of the entries of the column vector $\mathbf{F}^{R_S}_{XZ} = \mathbf{W}^R_X \mathbf{F}^{R_A}_{XZ}$ with Z being either H or V, according to (1) and (2) and the previously described alignment and beamforming processes in Section II-A. For Rx, after the offline digital beamforming and summation of the active column patterns using the final complex weights in (3), the beam patterns are

$$\mathbf{F}^{R_S}_{\mathrm{HH}}(\phi) = \mathbf{W}^R_H \mathbf{F}^{R_A}_{\mathrm{HH}}(\phi) \quad \mathbf{F}^{R_S}_{\mathrm{HV}} = \mathbf{W}^R_H \mathbf{F}^{R_A}_{\mathrm{HV}}(\phi) \quad (10a)$$

$$\mathbf{F}^{R_S}_{\mathrm{VH}}(\phi) = \mathbf{W}^R_V \mathbf{F}^{R_A}_{\mathrm{VH}}(\phi) \quad \mathbf{F}^{R_S}_{\mathrm{VV}} = \mathbf{W}^R_V \mathbf{F}^{R_A}_{\mathrm{VV}}(\phi). \quad (10b)$$

Examples of these patterns are presented in the next section. The Tx pattern situation is very similar, but the summation is performed electromagnetically through what is ideally a linear superposition of the measured element patterns, as described in Section II-A; however, as noted therein and unlike the Rx digital beamforming, there are limitations to the accuracy of both the weighting and superposition processes.

6) Optional (Polarimetric Correction): Because digital beamforming accuracy on Rx has precision and flexibility that is practically limited only by polarimetric measurement accuracy [18], it is also possible to perform polarimetric correction (PC) of the pattern, as was demonstrated in [19]. If the polarimetric Rx pattern for the pth active sector is given by

$$\mathbf{F}^{R_S}_p(\phi) = \begin{bmatrix} F^{R_S}_{\mathrm{HH},p}(\phi) & F^{R_S}_{\mathrm{HV},p}(\phi) \\ F^{R_S}_{\mathrm{VH},p}(\phi) & F^{R_S}_{\mathrm{VV},p}(\phi) \end{bmatrix} \quad (11)$$

with the additional subscript p denoting the pth column of the terms in (10), then the corrected polarimetric pattern is given by

$$\mathbf{F}^{R_C}_p(\phi) = \begin{bmatrix} F^{R_S}_{\mathrm{HH},p}(\phi_p) & F^{R_S}_{\mathrm{HV},p}(\phi_p) \\ F^{R_S}_{\mathrm{VH},p}(\phi_p) & F^{R_S}_{\mathrm{VV},p}(\phi_p) \end{bmatrix}^{-1} \mathbf{F}^{R_S}_p(\phi) \quad (12)$$

with ϕ_p being the center of the pth sector. The leftmost matrix and its inverse are very close to being diagonal, and for a CPPAR make only slight corrections to the received polarization. This operation not only ensures matching of the copolarized beams at the beam center but also ensures that the cross-polarized patterns exhibit a null at the AZ and EL beam center, corresponding to an ideal result for any CPPAR or PPPAR. The CPPAR naturally exhibits exceptionally low cross polarization relative to PPPAR equivalents [23], but matching of copolarized patterns at each scan angle is still important. Fig. 7 exemplifies the effects of these corrections at the beam center. In order to ensure that the measured results presented in the following section reflect the nominal performance of the CPPAR demonstrator (and not the the measurement setup itself), PC is performed at the beam center on all Rx results after this initial illustration. This is equivalent to the assumption that the polarization bases established by the far-field horns are "perfect" during the measurement process, which is the best reference available at the time of the measurements taken.

IV. Measurement Results

During the early measurement campaign on the CPPAR demonstrator, the above calibration and synthesis procedures were applied on both Tx and Rx to measure the resulting patterns. In this section, these patterns are qualified relative to the overall goals of the MPAR program and the challenges and trade spaces outlined in Tables I and II, respectively.

[3] See also footnote 1.

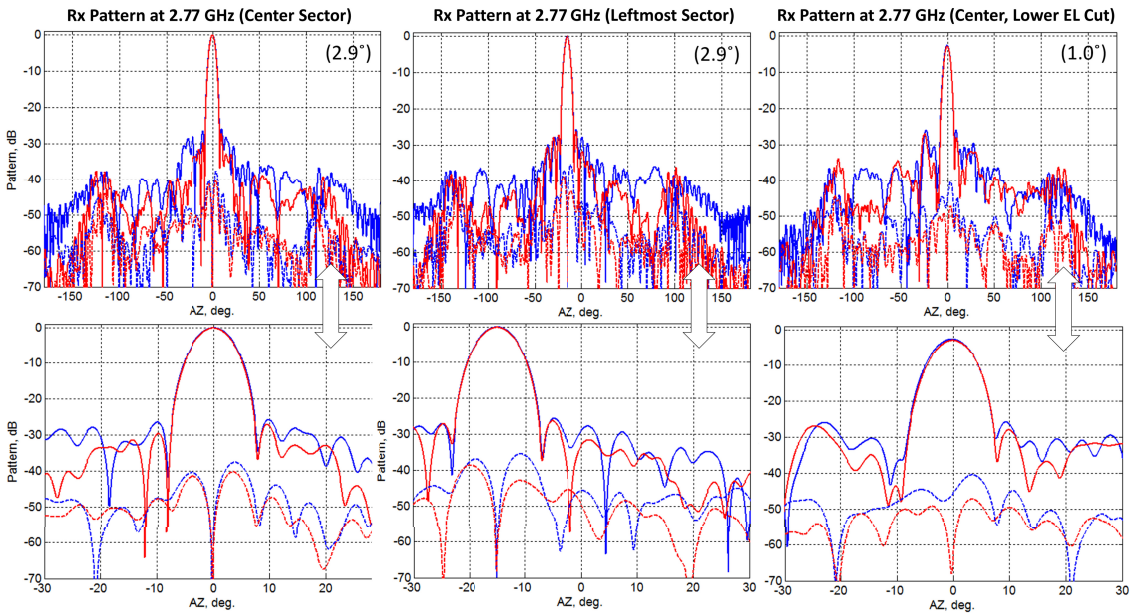

Fig. 8. Rx patterns at 2.77 GHz and a 2.9° EL. (Left) Center sector. (Middle) Leftmost sector. (Right) Center sector at a lower EL angle.

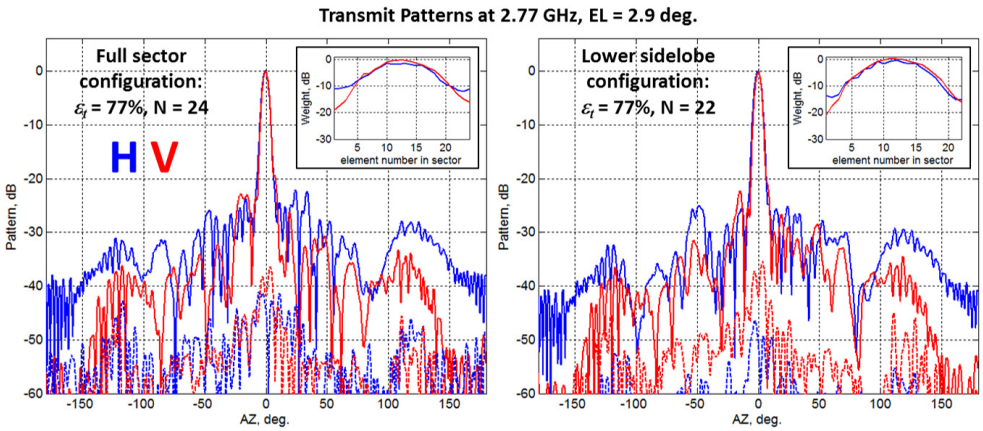

Fig. 9. Tx patterns for (left) 24 active columns and (right) 22 active columns, showing good matching between H and V copolarized patterns with naturally low cross-polarized characteristics. Resolution does not improve by increasing the number of active columns without degrading peak sidelobes in the far-out regions.

Before presenting the resulting patterns, it should be noted that they have been "filtered" to account for the fact that the summation in (5) can be truncated to $n_{max} \approx 1.1k_0r$ phase modes for a propagation constant $k_0 = 2\pi/\lambda_0$ and a cylindrical radius of r, owing to the nature of the Hankel functions that describe radiation from cylinders [20]. In these results, a phase mode filter (PMF) with a Tukey window-based bandwidth of $1.5k_0r$ phase modes has been implemented in order to conservatively remove all noise- and multipath-related ("non-CPPAR") components from the resulting measurements. An example of the effect of this processing as well as the polarization correction described in the previous section is shown in Fig. 7. It can be seen that PC modifies what is already a relatively low cross-polarized pattern to have a null at the beam center, while removal of the non-CPPAR radiation components through PMF reveals the smooth nature of the actual radiation patterns without fundamentally altering the beam characteristics.

Fig. 8 shows the middle and leftmost sector beam Rx patterns after the processing and calibration steps described in the previous sections, all at EL angles near the beam peak of the columns (2.9°). The patterns are also shown over a smaller AZ swath where, since the H and V patterns could be captured simultaneously using the turntable-based setup of Section II-A, the patterns demonstrate the real-time alignment and equalization of multiple H and V sector beams while simultaneously achieving low cross-polarization (with or without PC). Most importantly, it is clear that the overall beam shape and polarization characteristics remain invariant of the scan angle, a critical feature for accurate weather radar observations. The bottom row of Fig. 8 also shows that the beam quality is not significantly degraded when the exact same pattern is measured at an EL angle near the transition region of the beam (1.0°) along the EL dimension.

Fig. 9 shows the Tx patterns that were achieved with $N_T = 24$ and 22 columns, respectively, where with the same overall array efficiency very similar polarimetric characteristics were achieved. While the peak sidelobes were lower in the 22-column measurement, a slightly higher overall transmitted power density was achieved with the 24-column version (with

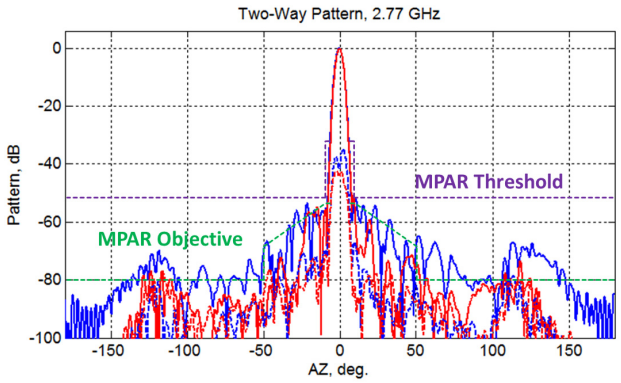

Fig. 10. Example two-way pattern compared with the MPAR threshold and objective levels.

more active columns) while preserving the overall matching between H and V copolarized patterns with naturally low cross-polarized patterns despite the lack of PC (as in the Rx case). However, the taper had to be more aggressive to achieve the indicated sidelobes. Correspondingly, beyond $N_T = 24$ columns, the peak sidelobe level near the grating lobe regions at approximately $\pm 120°$ increases beyond the worst case -28 dB exhibited in the leftmost of Fig. 9 without usefully decreasing the beamwidth (increasing resolution), making it more difficult to achieve the two-way sidelobe goals outlined in Table I. Because the 24-column pattern corresponds to a 90° active sector, this indicates that the CPPAR demonstrator's particular antenna geometry leads to resolution limits that correspond to a 90° sector. Solutions that seek to make use of larger active sectors (e.g., 120°) must ensure that grating lobe limitations do not lead to far-out sector isolation problems with the chosen element design and spacing. Simulations within the framework outlined in [25] should provide clear guidelines for such a behavior.

Finally, Fig. 10 shows an example of the achieved two-way polarimetric pattern—the calculated radar response to a perfectly spherical scattering target (e.g., the direct product of the polarimetric Tx and Rx patterns [18]). Here, PC is applied to Rx but not Tx. The pattern indicates that when scaled to the beamwidth of a full-scale MPAR, the CPPAR demonstrator nearly achieves the threshold cross-polarized and sidelobe goals for MPAR based on Table I, for both the more stringent simultaneous transmission case (simultaneous transmit, simultaneous receive) and the alternating transmission case (alternating transmit, simultaneous receive). Furthermore, with the exception of the grating lobes near $\pm 120°$, the pattern is nearly achieving the objective goals for the program, based on the polarimetric radar performance goals. The primary limitation, from an MPAR perspective, then appears to be front-to-back isolation, which would ideally be on the order of 80 dB for a *one-way* pattern. The extent to which the CPPAR demonstrator and other candidate CPPARs can achieve this goal remains a topic of further study.

V. Conclusion

There are no existing large-scale CPPAR systems that are available to explore the practical benefits and challenges of a cylindrical approach to the national multifunction PAR (MPAR) initiative. For the first time, this paper describes the design, calibration approach, and preliminary data analysis of such a system, the CPPAR demonstrator. As such, this paper addresses not only questions about practically achievable polarization and beam shape accuracies but also CPPAR-specific system-level practical challenges. Cylindrical arrays can be impacted by the potential of strong surface and creeping wave effects as well as the difficulty of achieving low sidelobes. Even from a pattern-only perspective that neglects the system-level implications of transceiver electronics, backend architecture, calibration, and operational constraints, there are very few available large-array and pattern synthesis techniques for complex antenna element geometries within a cylindrical array framework. This makes it difficult to even simulate electromagnetically accurate cylindrical array patterns in an ideal system. Hence, our CPPAR demonstrator allows for many open challenges to be studied in a way that would not otherwise be possible.

Acknowledgment

The authors would like to thank the students J. Kurdzo, L. Lei, D. Thompson, R. Lebron, A. Manccini, F. Nai, K. Williams, I. Meier, J. Christian, and R. Norris, who were involved in the development and integration of the CPPAR demonstrator, for their contributions.

References

[1] A. Shapiro, P. Robinson, J. Wurman, and J. Gao, "Single-Doppler velocity retrieval with rapid-scan radar data," *J. Atmos. Ocean. Technol.*, vol. 20, no. 12, pp. 1758–1775, 2003.

[2] A. L. Pazmany, J. B. Mead, H. B. Bluestein, J. C. Snyder, and J. B. Houser, "A mobile rapid-scanning X-band polarimetric (RaXPol) Doppler radar system," *J. Atmos. Ocean. Technol.*, vol. 30, no. 7, pp. 1398–1413, 2013.

[3] J. Wurman, "Preliminary results from the rapid-DOW, a multi-beam inexpensive alternative to phased arrays," in *Proc. 31st Conf. Radar Meteorol.*, 2003.

[4] D. S. Zrnić *et al.*, "Agile-beam phased array radar for weather observations," *Bull. Amer. Meteorol. Soc.*, vol. 88, pp. 1753–1766, 2007.

[5] M. M. Weber, J. Y. Cho, J. S. Herd, J. M. Flavin, W. E. Benner, and G. S. Torok, "The next-generation multimission U.S. surveillance radar network," *Bull. Amer. Meteorol. Soc.*, vol. 88, no. 11, pp. 1739–1751, 2007.

[6] G. Zhang, R. J. Doviak, D. S. Zrnić, J. E. Crain, D. Staiman, and Y. Al-Rashid, "Phased array radar polarimetry for weather sensing: A theoretical formulation for bias corrections," *IEEE Trans. Geosci. Remote Sens.*, vol. 47, no. 11, pp. 3679–3689, Nov. 2009.

[7] R. L. Jordan, B. L. Huneycutt, and M. Werner, "The SIR-C/X-SAR synthetic aperture radar system," *IEEE Trans. Geosci. Remote Sens.*, vol. 33, no. 4, pp. 829–839, Jul. 1995.

[8] R. J. Doviak, V. Bringi, A. Ryzhkov, A. Zahrai, and D. Zrnić, "Considerations for polarimetric upgrades to operational WSR-88D radars," *J. Atmos. Ocean. Technol.*, vol. 17, no. 3, pp. 257–278, 2000.

[9] C. Fulton, J. Herd, S. Karimkashi, G. Zhang, and D. S. Zrnić, "Dual-polarization challenges in weather radar requirements for multifunction phased array radar," in *Proc. IEEE Int. Symp. Phased Array Syst. Technol.*, Oct. 2013, pp. 494–501.

[10] J. L. Salazar, E. J. Knapp, and D. J. McLaughlin, "Dual-polarization performance of the phase-tilt antenna array in a CASA dense network radar," in *Proc. IEEE Int. Geosci. Remote Sens. Symp. (IGARSS)*, Jul. 2010, pp. 3470–3473. [Online]. Available: http://ieeexplore.ieee.org/lpdocs/epic03/wrapper.htm?arnumber=5650310

[11] NOAA Observing Systems Council, "NOAA/national weather service radar functional requirements," NOAA, Silver Spring, MD, USA, Tech. Rep., 2015.

[12] D. S. Zrnić, R. Doviak, G. Zhang, and A. Ryzhkov, "Bias in differential reflectivity due to cross coupling through the radiation patterns of polarimetric weather radars," *J. Atmos. Ocean. Technol.*, vol. 27, no. 10, pp. 1624–1637, 2010.

[13] G. Zhang, *Weather Radar Polarimetry*. Boca Raton, FL, USA: CRC Press, 2016.
[14] G. E. Crain and D. Staiman, "Polarization selection for phased array weather radar," in *Proc. AMS 23rd Conf. IIPS Annu. Meeting*, 2007, pp. 1–9.
[15] L. Lei, G. Zhang, R. J. Doviak, and S. Karimkashi, "Comparison of theoretical biases in estimating polarimetric properties of precipitation with weather radar using parabolic reflector, or planar and cylindrical arrays," *IEEE Trans. Geosci. Remote Sens.*, vol. 53, no. 8, pp. 4313–4327, Aug. 2015.
[16] D. S. Zrnić, G. Zhang, and R. J. Doviak, "Bias correction and Doppler measurement for polarimetric phased-array radar," *IEEE Trans. Geosci. Remote Sens.*, vol. 49, no. 2, pp. 843–853, Feb. 2011.
[17] L. Lei, G. Zhang, and R. J. Doviak, "Bias correction for polarimetric phased-array radar with idealized aperture and patch antenna elements," *IEEE Trans. Geosci. Remote Sens.*, vol. 51, no. 1, pp. 473–486, Jan. 2013.
[18] C. Fulton and W. Chappell, "Calibration of panelized polarimetric phased array radar antennas: A case study," in *Proc. IEEE Int. Symp. Phased Array Syst. Technol. (ARRAY)*, Oct. 2010, pp. 860–867.
[19] C. Fulton and W. J. Chappell, "Calibration of a digital phased array for polarimetric radar," in *IEEE MTT-S Int. Microw. Symp. Dig.*, May 2010, pp. 161–164.
[20] L. Josefsson and P. Persson, *Conformal Array Antenna Theory Design*. Hoboken, NJ, USA: Wiley, 2006.
[21] G. Zhang, R. J. Doviak, D. S. Zrnić, R. D. Palmer, L. Lei, and Y. Al-Rashid, "Polarimetric phased-array radar for weather measurement: A planar or cylindrical configuration?" *J. Atmos. Ocean. Technol.*, vol. 28, no. 1, pp. 63–73, 2011.
[22] C. Fulton, G. Zhang, W. Bocangel, L. Lei, R. Kelley, and M. McCord, "Cylindrical polarimetric phased array radar: A multi-function demonstrator and its calibration," in *Proc. IEEE Int. Conf. Microw., Commun., Antennas Electron. Syst. (COMCAS)*, Oct. 2013, pp. 1–5.
[23] S. Karimkashi and G. Zhang, "A dual-polarized series-fed microstrip antenna array with very high polarization purity for weather measurements," *IEEE Trans. Antennas Propag.*, vol. 61, no. 10, pp. 5315–5319, Oct. 2013.
[24] H. S. Mir and L. Albasha, "A low-cost high-performance digital radar test bed," *IEEE Trans. Instrum. Meas.*, vol. 62, no. 1, pp. 221–229, Jan. 2013.
[25] C. Fulton, "Phase mode analysis of a cylindrical polarimetric phased array antenna," in *Proc. Allerton Antenna Appl. Symp.*, Sep. 2014.
[26] D. Thompson, R. Kelley, M. Yeary, and J. Meier, "Direct digital synthesizer architecture in multichannel, dual-polarization weather radar transceiver modules," in *Proc. IEEE Radar Conf. (RADAR)*, May 2011, pp. 859–864.
[27] J. R. G. Oya, F. Munoz, A. Torralba, A. Jurado, A. J. Garrido, and J. Banos, "Data acquisition system based on subsampling for testing wideband multistandard receivers," *IEEE Trans. Instrum. Meas.*, vol. 60, no. 9, pp. 3234–3237, Sep. 2011.
[28] M. Yeary, R. Kelley, J. Meier, S. Ong, and R. Palmer, "Compact digital receiver development for radar based remote sensing," in *Proc. IEEE Instrum. Meas. Technol. Conf. (IMTC)*, May 2008, pp. 1761–1765.
[29] J. Meier, R. Kelley, B. M. Isom, M. Yeary, and R. D. Palmer, "Leveraging software-defined radio techniques in multichannel digital weather radar receiver design," *IEEE Trans. Instrum. Meas.*, vol. 61, no. 6, pp. 1571–1582, Jun. 2012.
[30] A. D. Yaghjian, "An overview of near-field antenna measurements," *IEEE Trans. Antennas Propag.*, vol. 34, no. 1, pp. 30–45, Jan. 1986.
[31] C. Fulton and W. Chappell, "Calibration techniques for digital phased arrays," in *Proc. IEEE Int. Conf. Microw., Commun., Antennas Electron. Syst. (COMCAS)*, Nov. 2009, pp. 1–10.
[32] D. Bekers, R. van Dijk, and F. van Vliet, "Mutual-coupling based phased-array calibration: A robust and versatile approach," in *Proc. IEEE Int. Symp. Phased Array Syst. Technol.*, Oct. 2013, pp. 630–637.
[33] A. Mitchell, "Coupling-based wideband digital phased array calibration techniques," M.S. thesis, School Elect. Comput. Eng., Univ. Oklahoma, Norman, OK, USA, 2014.
[34] C. Fulton, M. Yeary, D. Thompson, J. Lake, and A. Mitchell, "Digital phased arrays: Challenges and opportunities," *Proc. IEEE*, vol. 104, no. 3, pp. 487–503, Mar. 2016.
[35] A. O. Boryssenko, "Polarization constraints in dual-polarized phased arrays derived from an infinite current sheet model," *IEEE Antennas Wireless Propag. Lett.*, vol. 8, pp. 955–958, 2009.
[36] S. Karimkashi and G. Zhang, "Optimizing radiation patterns of a cylindrical polarimetric phased-array radar for multimissions," *IEEE Trans. Geosci. Remote Sens.*, vol. 53, no. 5, pp. 2810–2818, May 2015.
[37] C. J. Fulton and A. Mirkamali, "A computer-aided technique for the analysis of embedded element patterns of cylindrical arrays [EM programmer's notebook]," *IEEE Antennas Propag. Mag.*, vol. 57, no. 3, pp. 132–138, Jun. 2015.
[38] R. Mailloux, *Phased Array Antenna Handbook*, 2nd ed. Norwood, MA, USA: Artech House, 2005.
[39] O. M. Bucci, G. Franceschetti, G. Mazzarella, and G. Panariello, "Intersection approach to array pattern synthesis," *IEE Proc. H-Microw., Antennas Propag.*, vol. 137, no. 6, pp. 349–357, Dec. 1990.
[40] O. M. Bucci, G. Mazzarella, and G. Panariello, "Reconfigurable arrays by phase-only control," in *Dig. Antennas Propag. Soc. Int. Symp. (AP-S)*, vol. 1. Jun. 1989, pp. 142–145.

Caleb Fulton (S'05–M'11–SM'16) received the B.S. and Ph.D. degrees in electrical and computer engineering (ECE) from Purdue University, West Lafayette, IN, USA, in 2006 and 2011, respectively.

He is currently an Assistant Professor in ECE with the Advanced Radar Research Center, The University of Oklahoma, Norman, OK, USA. He is involved in antenna design, digital phased array calibration and compensation for transceiver errors, calibration for high-quality polarimetric radar measurements, integration of low-complexity transceivers and high-power GaN devices, and advanced digital beamforming design considerations, and in a number of digital phased array research and development efforts for a variety of applications.

Dr. Fulton is a member of the IEEE Antennas and Propagation Society, the IEEE Aerospace and Electronic Systems Society, and the IEEE Microwave Theory and Techniques Society. He also serves on the Education Committee of the latter. He was a recipient of the Purdue University Eaton Alumni Award for Design Excellence in 2009 for his work on the Army Digital Array Radar Project, the Meritorious Paper Award for a summary of these efforts at the 2010 Government Microcircuit Applications and Critical Technologies Conference, and the 2015 DARPA Young Faculty Award for his ongoing digital phased array research.

Jorge L. Salazar (S'00–M'12–SM'14) received the M.S. degree in electrical engineering from the University of Puerto Rico, Mayaguez, PR, USA, in 2003, and the Ph.D. degree from the University of Massachusetts, Amherst, MA, USA, in 2012.

In 2012, he received a prestigious National Center for the Atmospheric Research Advanced Study Program Post-Doctoral Fellowship. In 2012, he joined the Department of Electrical and Computer Engineering, University of Puerto Rico, as an Adjunct Professor. In 2012, he also joined the Advanced Radar Research Center and the Department of Electrical and Computer Engineering, The University of Oklahoma, Norman, OK, USA, as a Research Scientist and then became an Assistant Professor. His research interests include radar for microwave remote sensing, active phased array radars, antenna design, T/R modules, and electromagnetic scattering and propagation.

Dr. Salazar is a member of the Tau Beta Pi Honor Society of the IEEE TRANSACTIONS ON GEOSCIENCE AND REMOTE SENSING, the IEEE TRANSACTIONS ON ANTENNAS AND PROPAGATION, and the *IEEE Aerospace and Electronic Systems Magazine*.

Yan Zhang (M'03–SM'14) received the Ph.D. degree in electrical engineering from the University of Nebraska, Lincoln, NE, USA, in 2004.

On phased array radar developments, he led the CPPAR system development program during 2010–2011, Conformal Phased Array Demonstrator from 2011 to 2015, and various developments on intelligent calibrations, real-time adaptive array backend and processing, beam pattern optimizations, and reflect arrays for both ground based and airborne array applications. Since 2004, he has been involved in innovative radar research including phased array radars, airborne radars, and various low-probability of intercept radars. He is currently a Presidential Professor with The University of Oklahoma, Norman, OK, USA, where he is the Faculty Adviser for Intelligent Aerospace Radar Team and a Faculty Member of the Advanced Radar Research Center.

Guifu Zhang (S'97–M'98–SM'02) received the B.S. degree in physics from Anhui University, Hefei, China, in 1982, the M.S. degree in radio physics from Wuhan University, Wuhan, China, in 1985, and the Ph.D. degree in electrical engineering from the University of Washington, Seattle, WA, USA, in 1998.

From 1985 to 1993, he was an Assistant and an Associate Professor with the Space Physics Department, Wuhan University. In 1989, he joined the Communication Research Laboratory, Tokyo, Japan, as a Visiting Scholar. From 1993 to 1998, he was a Visiting Scientist with the Department of Electrical Engineering, University of Washington. He was a Scientist with the National Center for Atmospheric Research, Boulder, CO, USA, during 1998–2005. Then, he was with the School of Meteorology, The University of Oklahoma, Norman, OK, USA, where he is currently a Professor. He modeled and calculated wave scattering from fractal trees, and that from a target buried under a rough surface. He explored the detection of targets in the presence of clutter using angular correlation functions. He developed algorithms for retrieving raindrop size distributions. He led the development of advanced signal processing to improve weather radar data quality. He formulated theory of weather radar interferometry and that of phased array radar polarimetry. He has authored over 100 journal papers and a book, and holds three U.S. patent awards, including one on the Cylindrical Polarimetric Phased Array Radar, and filed more than ten intellectual property disclosures. His research interests include wave propagation and scattering in random and complex media, remote sensing theory and technology for geophysical applications, algorithms for retrieving physical states and processes, cloud and precipitation microphysics and model parameterization, target detection and classification, clutter identification and filtering, radar signal processing, and optimal estimation, and also the design and development of polarimetric phased array radars for weather measurements and multimission capability, as well as weather radar polarimetry.

Redmond Kelly received the bachelor's and master's degrees in electrical engineering from The University of Oklahoma (OU), Norman, OK, USA, in 2007 and 2009, respectively.

He has been a Staff Engineer with the Advanced Radar Research Center, OU, since 2009. He began his research in IF-sampling digital radar receiver technology and has since broadened his focus on radar hardware systems development. He supports most of the ARRC's hardware research projects and specializes in system level design/integration, analog/digital circuit design, and multilayer printed circuit board layout/fabrication/assembly. His research interests include the design of cost-effective conventional, imaging, and phased array radar technologies.

John Meier received the M.S. degree in electrical engineering from The University of Oklahoma (OU), Norman, OK, USA, in 2009.

He has been a Radar Engineer with the Advanced Radar Research Center, OU, since 2009, where he is involved in designing, building, and testing scalable digital phased array radar systems to achieve unparalleled levels of performance. He specializes in digital transceiver design, reprogrammable embedded processing and high-bandwidth, and low-latency network communication systems. His research interests include digital signal processing as well as radar control and scalable software control architectures.

Matt McCord received the B.S. degree in computer engineering and the M.S. degree in electrical engineering from The University of Oklahoma, Norman, OK, USA, in 2008 and 2012, respectively.

From 2012 to 2014, he was with the National Severe Storms Laboratory, Radar Research and Development Division, Norman. In 2014, he joined the Advanced Radar Research Center, The University of Oklahoma, as a Radar Engineer, specializing in digital transceivers and radar hardware for next generation phased array radars.

Damon Schmidt received the B.S. degree in mechanical engineering from the University of South Florida, Tampa, FL, USA, in 1987.

He is currently a Senior Principal Engineer with the Advanced Radar Research Center, The University of Oklahoma (OU), Norman, OK, USA. He has nearly thirty years of electromechanical systems engineering development experience including leading the full production WSR-88D antenna pedestal system development and currently his designs support active fleet operations in Canada, USA, and South Korea. He designed and led the manufacturing of the CPPAR mobility platform and antenna system and is currently heading up the mechanical design effort for OU-ARRC's all digital MPAR offering. He has extensive experience in CAD/CAM, and in the construction and management of complex technical data packages.

Andrew D. Byrd (S'05) received the B.S. degree in electrical engineering from the Georgia Institute of Technology, Atlanta, GA, USA, in 2014. He is currently pursuing the M.S. and Ph.D. degrees in electrical and computer engineering with The University of Oklahoma (OU), Norman, OK, USA.

He is currently a Graduate Research Assistant with the Advanced Radar Research Center, OU. His research interests include the design, calibration, and applications of polarimetric phased array radars.

Lal Mohan Bhowmik (S'06) received the B.Sc. degree in electronics and communication engineering from the Khulna University of Engineering and Technology, Khulna, Bangladesh, and the M.S. degree in electrical engineering from the South Dakota School of Mines and Technology, Rapid City, SD, USA, in 2012. He is currently pursuing the Ph.D. degree in electrical and computer engineering with The University of Oklahoma (OU), Norman, OK, USA.

He is currently a Graduate Research Assistant with the Advanced Radar Research Center, OU. His research interests include the analysis, design, and measurement of phased array antennas; flexible conformal antennas; frequency selective surfaces and artificial electromagnetic materials; electromagnetic materials characterization; ultrawideband antenna miniaturization; and radar cross section.

Mr. Bhowmik is currently a Student Member of the IEEE Antennas and Propagation and Microwave Theory and Techniques Societies.

Shaya Karimkashi (S'08–M'11) received the B.S. degree in electrical engineering from the K. N. Toosi University of Technology, Tehran, Iran, in 2003, the M.S. degree in electrical engineering from the University of Tehran, Tehran, in 2006, and the Ph.D. degree in electrical engineering from the University of Mississippi, Oxford, MS, USA, in 2011.

From 2011 to 2015, he was with the Advanced Radar Research Center, The University of Oklahoma, Norman, OK, USA, where he was a Post-Doctoral Fellow and later became a Research Scientist and an Adjunct Assistant Professor. He joined the Space Exploration Technologies Corporation, Hawthorne, CA, USA, in 2015. He has authored over 40 referred journal and conference papers. His research interests include the area of antenna arrays, phased array systems, focused antennas, based station antennas, computer aided design for antennas, and optimization techniques in electromagnetics.

Dr. Karimkashi is currently a member of the IEEE Antennas and Propagation, Phi Kappa Phi, and Sigma Xi societies.

Dusan S. Zrnic (M'73–SM'77–F'90–LF'08) received the bachelor's degree from the University of Belgrade, Belgrade, Serbia, in 1965, and the M.S. and Ph.D. degrees from the University of Illinois at Urbana–Champaign, Champaign, IL, USA, in 1966 and 1969, respectively.

He is currently a Senior Scientist with the National Severe Storms Laboratory, Norman, OK, USA, and an Affiliate Professor of Meteorology and Electrical Engineering, The University of Oklahoma, Norman. He has developed several scientific and engineering aspects of polarimetric weather radar technology leading to implementation on the WSR-88Ds. He was inducted into the U.S. National Academy of Engineering in 2006 for the development of potent radar methods that have greatly enhanced operational weather detection and warning and advanced meteorological research.

Dr. Zrnic is currently a Fellow of AMS. He was a recipient of the AMS Remote Sensing Prize in 2008 for pioneering and substantial contributions to the improvements of meteorological radars for both research and operational applications. He was the Chief Editor of the *Journal of Atmospheric and Oceanic Technology*.

Richard J. Doviak (S'56–M'57–SM'72–F'90–LF'97) received the B.S.E.E. degree from the Rensselear Polytechnic Institute, Troy, NY, USA, and the M.Sc. and Ph.D. degrees from the University of Pennsylvania, Philadelphia, PA, USA.

He was responsible for leading a project to develop 10 cm Doppler weather radars that became the prototype used by the National Weather Service at the National Severe Storms Laboratory (NSSL), Norman, OK, USA. He has been a Visiting Professor at Kyoto University, Kyoto, Japan, and Australian National University, Canberra, ACT, Australia. He is currently a Senior Engineer with NSSL and an Affiliated Professor with the Department of Electrical Engineering and Meteorology, The University of Oklahoma, Norman.

Dr. Doviak is currently a Fellow of the Cooperative Institute for Mesoscale Meteorological Studies and the American Meteorological Society. He was an Associate Editor of the *Journal of Atmospheric and Oceanic Technology* and the *Journal of Applied Meteorology*, and the Editor of the IEEE TRANSACTIONS ON GEOSCIENCE AND REMOTE SENSING.

Allen Zahrai received the B.S. degree in electrical engineering with a minor in mathematics from The University of Oklahoma, Norman, OK, USA, in 1972, and the M.S. degrees in electrical engineering and computer science, The University of Oklahoma in 1974 and 1984, respectively.

He was on joint projects as a Graduate Research Assistant with the National Severe Storms Laboratory, Norman, in 1973 and 1974, where he was an Electronics Engineer in 1975. His primary responsibility was the design and implementation of real-time digital signal processing circuits and systems for Doppler weather radars, leading to the national weather radar network; WSR-88D (NEXRAD). He is currently the Radar Engineering and Development Team Leader with the Radar Research and Development Division, National Severe Storms Laboratory, where he leads the development and maintenance of atmospheric remote sensing equipment. He has authored numerous technical articles and journal papers. He is actively involved in the development and evaluation of dual-polarized active electronically scanned arrays and their application to radar meteorology.

Mr. Zahrai was a recipient of many awards including a Bronze Medal for the development of one of the first dual-polarized Doppler weather radars in 1994.

Mark Yeary (S'95–M'00–SM'03–F'16) received the B.S. (Hons.), M.S., and Ph.D. degrees from the Department of Electrical Engineering, Texas AM University, College Station, TX, USA, in 1992, 1994, and 1999, respectively.

From 2002 to 2016, he was at Raytheon, Dallas, TX, USA. He has served as a Principal Investigator (PI) or Co-PI on grants from NASA, NSF-ATM, NSFDUE, NSF-ECCS, DoD-EPSCoR, NOAA-CSTAR, NOAA-NSSL, Raytheon, DARPA (with Rockwell-Collins), and AFRL. Since 2002, he has been with the School of Electrical and Computer Engineering, The University of Oklahoma (OU), Norman, OK, USA, where he was named the endowed Hudson-Torchmark Presidential Professor in 2011. He is also one of the Founding Members of the Advanced Radar Research Center, OU. He is currently a Senior Engineer with Raytheon. His research interests include digital signal processing (DSP) as applied to customized DSP systems and instrumentation for radar systems with an emphasis on hardware prototype development and practical measurements.

Dr. Yeary is currently a member of the Tau Beta Pi and Eta Kappa Nu Honor societies. He received the Outstanding Young Engineer Award from the Institute of Electrical and Electronics Engineers (IEEE) in 2006. This award was given by the Instrumentation and Measurement Society of the IEEE. He is a licensed Professional Engineer.

Robert D. Palmer (S'86–M'89–SM'93–F'16) was born in Fort Benning, GA, USA, in 1962. He received the Ph.D. degree in electrical engineering from The University of Oklahoma (OU), Norman, OK, USA, in 1989.

From 1989 to 1991, he was a JSPS Post-Doctoral Fellow with the Radio Atmospheric Science Center, Kyoto University, Kyoto, Japan, where his major accomplishment was the development of novel interferometric radar techniques for studies of atmospheric turbulent layers. He was with the Physics and Astronomy Department, Clemson University, Clemson, SC, USA. From 1993 to 2004, he was a part of the faculty of the Department of Electrical Engineering, University of Nebraska, Lincoln, NE, USA, where his research interests include wireless communications, remote sensing, and pedagogy. He joined the School of Meteorology, OU, as the Tommy C. Craighead Chair in 2004, where he established the interdisciplinary Advanced Radar Research Center (ARRC). He currently serves as the Executive Director of the ARRC and an Associate Vice President for Research at OU. He has authored widely in the area of radar remote sensing of the atmosphere, with an emphasis on generalized imaging problems, spatial filter design, and clutter mitigation using advanced array/signal processing techniques. His research interests include the application of advanced radar signal processing techniques to observations of severe weather, particularly related to phased-array radars and other innovative system designs.

Prof. Palmer is a Fellow of the American Meteorological Society. He was a recipient of several awards for both his teaching and research accomplishments.